Triggered high-mass star formation in the H II region W 28 A2: A cloud–cloud collision scenario

Katsuhiro Hayashi [1,2,*] Satoshi Yoshiike,[1] Rei Enokiya [1]
Shinji Fujita [1,3] Rin Yamada,[1] Hidetoshi Sano [1,4,5] Kazufumi Torii,[6]
Mikito Kohno [1,7] Atsushi Nishimura [3] Akio Ohama,[1]
Hiroaki Yamamoto,[1] Kengo Tachihara,[1] Graeme Wong,[8,9]
Nigel Maxted [10,11] Catherine Braiding,[9] Gavin Rowell,[12]
Michael Burton,[13] and Yasuo Fukui[1,4]

[1]Department of Physics, Nagoya University, Chikusa-ku, Nagoya, Aichi 464-8602, Japan

[2]Institute of Space and Astronautical Science (ISAS), Japan Aerospace Exploration Agency (JAXA), 3-1-1 Yoshinodai, Chuo-ku, Sagamihara, Kanagawa 252-5210, Japan

[3]Department of Physical Science, Graduate School of Science, Osaka Prefecture University, 1-1 Gakuen-cho, Naka-ku, Sakai, Osaka 599-8531, Japan

[4]Institute for Advanced Research, Nagoya University, Chikusa-ku, Nagoya, Aichi 464-8601, Japan

[5]National Astronomical Observatory of Japan, Mitaka, Tokyo 181-8588, Japan

[6]Nobeyama Radio Observatory, 462-2 Nobeyama Minamimaki-mura, Minamisaku-gun, Nagano 384-1305, Japan

[7]Astronomy Section, Nagoya City Science Museum, 2-17-1 Sakae, Naka-ku, Nagoya, Aichi 460-0008, Japan

[8]Pawsey Supercomputing Centre, 26 Dick Perry Ave, Kensington 6151, WA, Australia

[9]School of Physics, The University of New South Wales, Sydney 2052, Australia

[10]Western Sydney University, Locked Bag 1797, Penrith, NSW 2751, Australia

[11]School of Science, The University of New South Wales, Australian Defence Force Academy, Canberra 2610, Australia

[12]School of Physical Sciences, The University of Adelaide, Adelaide 5005, Australia

[13]Armagh Observatory and Planetarium, College Hill, Armagh BT61 9DG, UK

*E-mail: khayashi@a.phys.nagoya-u.ac.jp

Abstract

We report on a study of the high-mass star formation in the H II region W 28 A2 by investigating the molecular clouds that extend over $\sim$5–10 pc from the exciting stars using the ^{12}CO and ^{13}CO ($J = 1$–0) and ^{12}CO ($J = 2$–1) data taken by NANTEN2 and Mopra observations. These molecular clouds consist of three velocity components with CO intensity peaks at $V_{\rm LSR} \sim -4$ km s^{-1}, 9 km s^{-1}, and 16 km s^{-1}. The highest CO intensity is detected at $V_{\rm LSR} \sim 9$ km s^{-1}, where the high-mass stars with spectral types O6.5–B0.5 are embedded. We found bridging features connecting these clouds toward the directions of the exciting sources. Comparisons of the gas distributions with the radio continuum emission and 8 μm infrared emission show spatial coincidence/anti-coincidence, suggesting physical

associations between the gas and the exciting sources. The ^{12}CO $J = 2$–1 to 1–0 intensity ratio shows a high value ($\gtrsim 0.8$) toward the exciting sources for the $-4\,\mathrm{km\,s^{-1}}$ and $+9\,\mathrm{km\,s^{-1}}$ clouds, possibly due to heating by the high-mass stars, whereas the intensity ratio at the CO intensity peak ($V_{\mathrm{LSR}} \sim 9\,\mathrm{km\,s^{-1}}$) decreases to ~ 0.6, suggesting self absorption by the dense gas in the near side of the $+9\,\mathrm{km\,s^{-1}}$ cloud. We found partly complementary gas distributions between the $-4\,\mathrm{km\,s^{-1}}$ and $+9\,\mathrm{km\,s^{-1}}$ clouds, and the $-4\,\mathrm{km\,s^{-1}}$ and $+16\,\mathrm{km\,s^{-1}}$ clouds. The exciting sources are located toward the overlapping region in the $-4\,\mathrm{km\,s^{-1}}$ and $+9\,\mathrm{km\,s^{-1}}$ clouds. Similar gas properties are found in the Galactic massive star clusters RCW 38 and NGC 6334, where an early stage of cloud collision to trigger the star formation is suggested. Based on these results, we discuss the possibility of the formation of high-mass stars in the W 28 A2 region being triggered by cloud–cloud collision.

Key words: ISM: H II region — stars: formation — ISM: individual objects (W 28 A2)

1 Introduction

1.1 High-mass star formation

High-mass stars greatly influence the physical and chemical environments of the interstellar medium (ISM) by injecting considerable energy through stellar winds, ultraviolet (UV) radiation, and explosions of supernovae at the end of their lives. Material around the high-mass stars is ionized by the UV photons, creating various sizes and shapes of H II regions. Heavy elements produced by the supernova explosions affect the chemical evolution of the ISM. Revealing the formation process of high-mass stars is essential to understanding the physical properties of the ISM and the evolution of galaxies.

The early stage of star formation is generally explained by a contraction of the interstellar gas due to self-gravity in a turbulent medium. Theoretically, "core accretion" and "competitive accretion" are commonly invoked scenarios to explain the formation of massive stars (for reviews, see, e.g., Zinnecker & Yorke 2007; Tan et al. 2014). While these models assume a gravitationally bound system, possible scenarios of external agents triggering the formation of high-mass stars have been discussed (e.g., Elmegreen 1998). One of the triggering scenarios is the expanding motion of ionized gas ("collect and collapse"; e.g., Elmegreen & Lada 1977). The external pressure in a shock wave accumulates the surrounding material and forms gravitationally unstable dense cores, which collapse to create the next generation of stars. The other triggering scenario is collisions of molecular clouds ("cloud–cloud collision"; e.g., Loren 1979; Habe & Ohta 1992). The incidental collision of two clouds at a supersonic relative velocity accumulates the gas in a shock wave and generates a gravitationally unstable dense core, leading to the formation of a high-mass star.

A number of discoveries of Spitzer bubbles in the 2000s (Churchwell et al. 2006, 2007) established collect and collapse as a plausible model of the triggering of high-mass star formation (e.g., Sh 104: Deharveng et al. 2003; RCW 79: Zavagno et al. 2005). The size of the H II region in a bubble can be explained by the UV radiation from the central massive star, which promotes the next generation of stars at the peripheries of the H II region. This model is also supported by the theoretical aspects of the formation of the bubble structure (Hosokawa & Inutsuka 2006). However, a detailed explanation of the expanding gas motion of the ionized gas has not been found. The pressure from the H II region easily escapes from the surface of the molecular gas because the shape of the molecular clouds is flattened rather than symmetric (Beaumont & Williams 2010). Even if collect and collapse can be applied to sequential star formation, it does not explain the formation of the first-born central massive stars.

On the other hand, the model of cloud–cloud collision better explains these problems. The collision induces the formation of dense clumps in the compressed region, achieving a mass accretion rate large enough (10^{-4} to $10^{-3}\,M_{\odot}\,\mathrm{yr}^{-1}$) to create massive stars (e.g., Inoue & Fukui 2013; Takahira et al. 2014). If the collision occurs between clouds with different sizes along the line of sight, the smaller cloud creates a hole in the larger cloud, which forms a ring-like gas distribution (e.g., figure 12 in Torii et al. 2017). Depending on the angle and the elapsed time of the collision, the smaller cloud is displaced relative to the hole in the larger cloud. The UV radiation from the massive stars ionizes the surrounding gas and creates the infrared ring associated with the gas distribution (e.g., Torii et al. 2015). If the clouds are not dispersed by the ionization, they show a complementary gas distribution. The momentum exchange between the colliding clouds generates bridging structures in the position–velocity diagram.
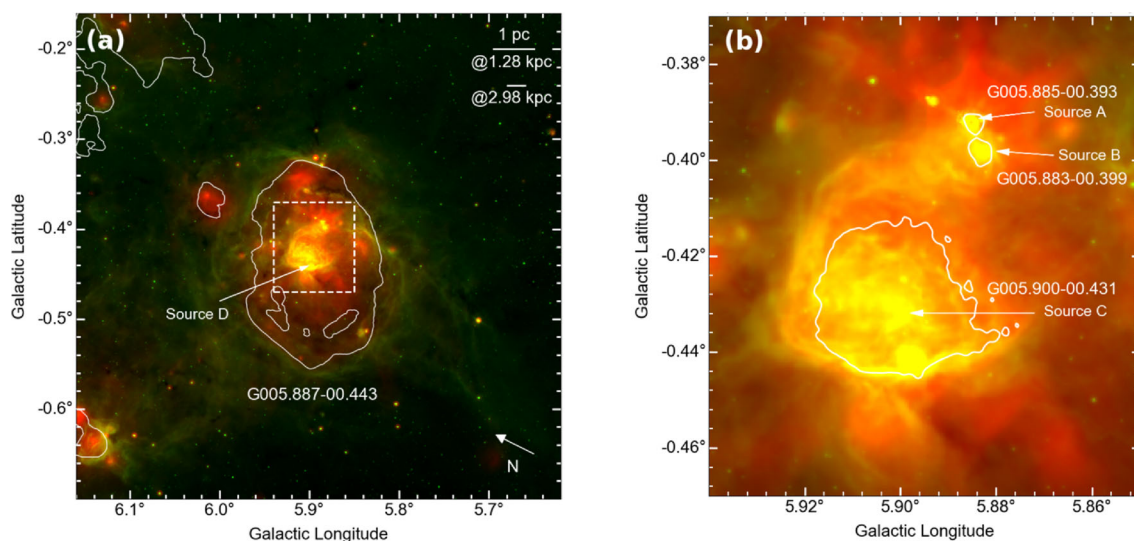
Fig. 1. Spitzer $8\,\mu$m (green) and $24\,\mu$m (red) images. The dashed box in panel (a) corresponds to the entire area of panel (b). The white contours show the fluxes of the radio continuum emission from the VLA 20 cm data, corresponding to 2 mJy beam^{-1} in panel (a), and 10 and 16 mJy beam^{-1} respectively for the H II regions of Source C and Sources A and B in panel (b).

Such cloud properties are found in several Galactic massive star clusters (e.g., Westerlund 2: Furukawa et al. 2009; Ohama et al. 2010; RCW 38: Fukui et al. 2016; M 42: Fukui et al. 2018a; NGC 6334/NGC 6357: Fukui et al. 2018b; NGC 6618: Nishimura et al. 2018) and H II regions which harbor one or more high-mass stars (e.g., RCW 120: Torii et al. 2015; G35.20−0.74: Dewangan 2017; RCW 32: Enokiya et al. 2018; RCW 36: Sano et al. 2018; RCW 34: Hayashi et al. 2018; S44: Kohno et al. 2021; N4: Fujita et al. 2019), as well as the active star-forming regions in the Large Magellanic Cloud and M 33 (e.g., Tachihara et al. 2018; Tsuge et al. 2019; Sano et al. 2021). Enokiya, Torii, and Fukui (2021) performed a statistical study using these observational findings and found that the peak gas column density becomes larger as the relative velocity between colliding clouds in the Galactic disk increases.

1.2 The H II complex W 28 A2

W 28 A2 is an H II complex region with bright radio continuum emission (Milne & Hill 1969; Goudis 1976), located ∼50′ away from the supernova remnant W 28. Figures 1a and 1b respectively show composite $8\,\mu$m and $24\,\mu$m images of this region, with contours indicating the VLA 20 cm radio continuum emission overlaid. Multiple H II regions are identified in the WISE catalog (Anderson et al. 2014). In the largest H II region, G005.887−00.443 with radius ∼0°.1, a compact H II region, G005.900−00.431, and two ultra-compact (UC) H II regions, G005.883−00.399 and G005.885−00.393, are included. Since W 28 A2 is located near the direction

of the Galactic center and thus suffers from much line-of-sight contamination, it is difficult to determine the distance accurately. The distance to the UC H II region G005.885−00.393 is estimated to be ∼2–4 kpc by kinematic studies (e.g., Acord et al. 1998; Fish et al. 2003) and 1.28 kpc (Motogi et al. 2011) or 2.98 kpc (Sato et al. 2014) by trigonometric parallax measurements with maser observations. Klaassen et al. (2006) investigated the molecular gas distribution in or around G005.885−00.393 within a 100″ scale and captured the broad CO emission line with a velocity up to ±50 km s^{-1}. Taking a ^{12}CS ($J = 1$–0) observation, Nicholas et al. (2012) found dense molecular gas toward the compact/UC H II regions and an extended arm feature of length 6′ on the northeast side of the H II region. They also detected Class I CH$_3$OH masers from the dense gas regions, suggesting the presence of shocks and outflows related to high-mass star formation. The detection of GeV and TeV γ-rays from the W 28 A2 region suggests the existence of rich gas, possibly related to the supernova remnant W 28 (e.g., Hanabata et al. 2014; Hampton et al. 2016). Velázquez et al. (2002) performed a large-scale study of H I emission toward this area and found a strong self-absorption feature in the spectrum at $V_{LSR} = 7$ km s^{-1}.

Among the H II regions in W 28 A2, G005.885−00.393 has been widely studied as a possible high-mass protostar (known as Feldt's star) with an extremely energetic molecular outflow (e.g., Acord et al. 1998; Feldt et al. 2003). Several interferometric molecular observations discovered at least three outflows from this area (Watson et al. 2007; Hunter et al. 2008; Su et al. 2012; see figure 1 in Leurini et al. 2015). The spectral type of the embedded exciting

star is inferred to be O or B-type zero-age main sequence (ZAMS; e.g., O5 or earlier, based on the infrared spectral measurements: Feldt et al. 2003; O8–O8.5, based on the Lyman continuum photons and the far-infrared luminosity: Motogi et al. 2011), but the estimate strongly depends on the distance adopted. An X-ray study by Hampton et al. (2016) derived the spectral type to be B5–B7, which is consistent with the lower limit given by Feldt et al. (2003). A short dynamical timescale of the ionized nebula ($\sim$600 yr) was inferred from the expanding ionized shell traced by the VLA measurements (Acord et al. 1998), and the outflow age was estimated to be 1300–5000 yr from measurements of the CO spectral lines (Motogi et al. 2011). These results indicate that G005.885−00.393 is very young system. While G005.885−00.393 has been investigated in detail to study star formation activity, the other H II regions have received less focus, and the possible relations between the H II regions are not understood. Furthermore, a wide molecular survey at a $\sim$0°.3 scale beyond the H II region has not yet been performed, and thus the physical associations between the massive stars and the surrounding gas in the entire W 28 A2 region is not clear.

In this paper we aim to investigate the molecular clouds in the W 28 A2 region and to look for a relationship between the gas dynamics and the star formation activity, mainly focusing on the models of triggered star formation introduced in subsection 1.1. We have used new ^{12}CO and ^{13}CO ($J = 1$–0) data and ^{12}CO ($J = 2$–1) data from NANTEN2 and Mopra observations with a scale of 0°.6 × 0°.6, as well as an archival data set of the Mopra ^{12}CS ($J = 1$–0) line,[1] VLA 20 cm radio continuum emission,[2] and Spitzer 8 μm and 24 μm emission.[3] This is the first study of a probable process of high-mass star formation in the W 28 A2 region based on the correlation between the H II regions and the surrounding gas. Because the distance to the W 28 A2 region is not clear, we have adopted two distances, 1.28 kpc (Motogi et al. 2011) and 2.98 kpc (Sato et al. 2014), which are the results from the recent trigonometric parallax measurements, and calculated the physical quantities in both cases. The different distances do not change our conclusion. We also assume that each H II region holds one exciting star, denoted as Source A, B, C, and D for the G005.885−00.393, G005.883−00.399, G005.900−00.431, and G005.887−00.443 areas, respectively.

The paper is organized as follows. Section 2 describes the data we used in the study. Section 3 shows the results, and section 4 discusses the possible mechanisms of high-mass

star formation in W 28 A2. Section 5 provides a summary of the study.

2 Observations

2.1 NANTEN2 ^{12}CO and ^{13}CO ($J = 1$–0), and ^{12}CO ($J = 2$–1) observations

Observations of the ^{12}CO and ^{13}CO ($J = 1$–0) lines toward the W 28 A2 region were made with the NANTEN2 millimeter/sub-millimeter telescope located at Atacama, Chile, in 2011 November. The frontend was a 4 K-cooled Nb superconductor–insulator–superconductor mixer receiver, which provided a system noise temperature including the atmosphere of $\sim$160 K in double sideband. The backend was a digital spectrometer with 16384 channels at 1 GHz bandwidth and the frequency resolution was 61 kHz, which corresponds to a velocity coverage of $\sim$2600 km s^{-1} and a velocity resolution of 0.16 km s^{-1} at 115 GHz. The pointing accuracy achieved was $<$100$''$ by observing IRC 10216 at (RA, Dec) = (09$^{\rm h}$47$^{\rm m}$57$^{\rm s}_{.}$4, 13°16$'$43$''_{.}$6) and the edge of the Sun. The absolute intensity calibration was made with a CO observation toward ρ-Ophiucus at (RA, Dec) = (16$^{\rm h}$19$^{\rm m}$20$^{\rm s}_{.}$9, −24°22$'$13$''_{.}$0). These data were smoothed to a beam size of 200$''$ (half-power beam width) with a Gaussian function and to a velocity resolution of 0.5 km s^{-1}. These corrections gave typical rms noise levels for the ^{12}CO and ^{13}CO ($J = 1$–0) lines of $\sim$0.3 K channel^{-1} and $\sim$0.5 K channel^{-1}, respectively.

The NANTEN2 ^{12}CO ($J = 2$–1) line observation toward W 28 A2 was made in 2008 November. The system noise temperature including the atmosphere was $\sim$200 K at 230 GHz in single side-band. The backend was the acoustic-optical spectrometer (AOS) with 2048 channels, which corresponds to a velocity coverage of 392 km s^{-1} with a velocity resolution of 0.38 km s^{-1}. The data were smoothed to a beam size of 100$''$ and a velocity resolution of 0.5 km s^{-1}, giving a typical noise level of $\sim$0.3 K channel^{-1}.

2.2 Mopra ^{12}CO and ^{13}CO ($J = 1$–0) observations

To investigate the gas distribution at greater spatial resolution we used the ^{12}CO and ^{13}CO ($J = 1$–0) lines obtained by the Mopra 22 m millimeter telescope of the CSIRO Australia Telescope National Facility. On-the-fly mapping observations toward W 28 A2 were conducted from 2016 April to July and from 2018 April to May as part of the Mopra Southern Galactic Plane CO Survey (Burton et al. 2013; Braiding et al. 2015, 2018). The SiO maser source VX Sgr was used to measure the pointing accuracy. The typical system noise temperature was $\sim$300–800 K in single
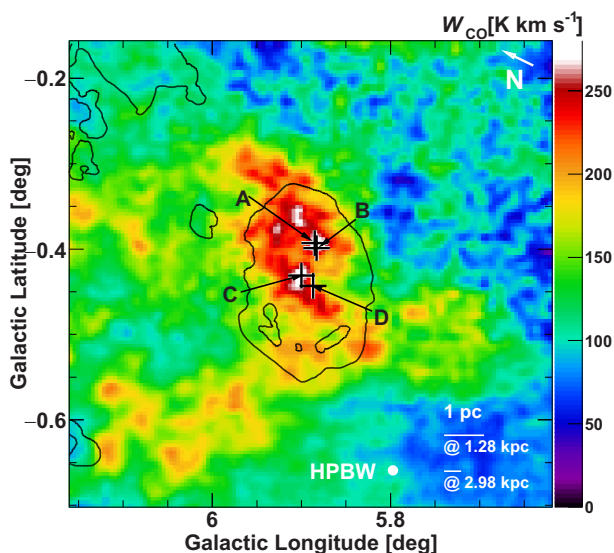
---

[1] ⟨http://www.physics.adelaide.edu.au/astrophysics/MopraGam/⟩.

[2] ⟨http://sundog.stsci.edu⟩.

[3] ⟨https://irsa.ipac.caltech.edu/data/SPITZER/GLIMPSE/⟩.

Fig. 2. Mopra ^{12}CO ($J = 1$–0) integrated intensity map with the velocity range -10 to $30 \, \mathrm{km \, s^{-1}}$. The contours indicate the intensity of the radio continuum emission from the VLA 20 cm data drawn in figure 1a. The crosses represent the positions of the exciting sources A–D.

side-band. We used the digital UNSW Mopra Spectrometer (MOPS), which provides data with a velocity resolution of $0.1 \, \mathrm{km \, s^{-1}}$ covering the velocity ranges $\sim 1100 \, \mathrm{km \, s^{-1}}$ and $\sim 770 \, \mathrm{km \, s^{-1}}$ for the ^{12}CO and ^{13}CO lines, respectively. To obtain the absolute intensity, we adopted an extended beam efficiency of $\eta = 0.55$ (Burton et al. 2013) for both lines. The original spatial resolution of the data $(36'')$ was smoothed to be $45''$. The velocity axis was smoothed to be $0.5 \, \mathrm{km \, s^{-1}}$, improving the noise level up to $\sim 0.6 \, \mathrm{K \, channel^{-1}}$ and $\sim 0.3 \, \mathrm{K \, channel^{-1}}$ for the ^{12}CO and ^{13}CO lines, respectively.

3 Results

3.1 Distribution of the molecular gas

We present the distribution of molecular clouds toward the H II region W 28 A2 using the NANTEN2 and Mopra CO data. Figure 2 shows a velocity-integrated intensity map of the Mopra ^{12}CO ($J = 1$–0) data, with the contours of the VLA radio continuum emission. The integrated velocity range is -10 to $30 \, \mathrm{km \, s^{-1}}$, which covers all the velocity components found by the NANTEN2 ^{12}CO ($J = 1$–0) and ($J = 2$–1) observations (figure 4). We found strong emission toward the H II regions and several clouds across the Galactic longitude direction in the area with $b \lesssim -0°\!\!.40$. Sources A and B are located close to the intensity peak at $(l, b) \sim (5°\!\!.89, -0°\!\!.40)$, and Sources C and D are close to another intensity peak at $(l, b) \sim (5°\!\!.90, -0°\!\!.43)$. The peak positional correspondence between the CO and radio

continuum emissions suggests that these exciting sources are embedded in the rich molecular gas. The diffuse molecular gas is widely distributed within ~ 5 pc (at 1.28 kpc) or ~ 10 pc (at 2.98 kpc) of the exciting stars, beyond the extent of the radio continuum emission (black contour), partly showing anti-correlation with the H II regions located at $(l, b) \sim (6°\!\!.15, -0°\!\!.65)$ and $(6°\!\!.12, -0°\!\!.25)$— see also figure 1a.

Figure 3 shows a velocity channel map obtained from the Mopra ^{12}CO ($J = 1$–0) data. From the morphological structure, we found three gas components separated by velocity: low-intensity components elongated to the Galactic north–south direction in the channel maps of $-6 < V_{\mathrm{LSR}} < 0 \, \mathrm{km \, s^{-1}}$; high-intensity components covering the positions of Sources A–D at $V_{\mathrm{LSR}} \sim +9 \, \mathrm{km \, s^{-1}}$; and multiple components distinctly distributed at $12 \, \mathrm{km \, s^{-1}} \lesssim V_{\mathrm{LSR}}$, with the highest intensity at $V_{\mathrm{LSR}} \sim +16 \, \mathrm{km \, s^{-1}}$. We hereafter denote these three molecular clouds separated by velocity as the $-4 \, \mathrm{km \, s^{-1}}$ cloud, the $+9 \, \mathrm{km \, s^{-1}}$ cloud, and the $+16 \, \mathrm{km \, s^{-1}}$ cloud, whose velocity ranges are determined by eye as -6 to $-1 \, \mathrm{km \, s^{-1}}$, $+4$ to $+12 \, \mathrm{km \, s^{-1}}$, and $+14$ to $+24 \, \mathrm{km \, s^{-1}}$, respectively. This molecular gas extends over the intermediate velocity range ($V_{\mathrm{LSR}} \sim -1$ to $+4 \, \mathrm{km \, s^{-1}}$ and $\sim +12$ to $+14 \, \mathrm{km \, s^{-1}}$). Modifying the velocity range within $\sim \pm 1 \, \mathrm{km \, s^{-1}}$ does not affect our discussion.

The $-4 \, \mathrm{km \, s^{-1}}$ cloud extended to the eastern (negative latitude) side has not been recognized in previous studies of the W 28 A2 region. The positional correspondence of the CO peaks at $+9 \, \mathrm{km \, s^{-1}}$ with the exciting sources A–D suggests that these stars are embedded in the $+9 \, \mathrm{km \, s^{-1}}$ cloud. This result is consistent with previous molecular observations (Klaassen et al. 2006; Nicholas et al. 2012). The $+16 \, \mathrm{km \, s^{-1}}$ cloud has two CO peaks, one of which, located in the eastern area, is possibly associated with another H II region at $(l, b) \sim (6°\!\!.15, -0°\!\!.65)$—see figure 1a. We also found a ring-like structure centered on $(l, b) \sim (6°\!\!.05, -0°\!\!.35)$ at $V_{\mathrm{LSR}} \sim +16 \, \mathrm{km \, s^{-1}}$, and Sources A–D are positioned at the the rim of the ring, close to one of the CO peaks at $(l, b) \sim (5°\!\!.83, -0°\!\!.52)$, which is part of the largely elongated clouds from the northeast to the southwest.

Figures 4a and 4b show ^{12}CO ($J = 1$–0, $J = 2$–1) and ^{13}CO ($J = 1$–0) spectra obtained by the NANTEN2 observations toward Sources A and C, respectively. The three velocity components are confirmed in the spectra for Source C. The spectra for Source A have peaks at $V_{\mathrm{LSR}} \sim 9 \, \mathrm{km \, s^{-1}}$ and $\sim 16 \, \mathrm{km \, s^{-1}}$, but the ^{12}CO lines at $V_{\mathrm{LSR}} \sim -4 \, \mathrm{km \, s^{-1}}$ exhibit wing-like shapes rather than peaking structures. We do not detect significant ^{13}CO ($J = 1$–0) emission at $V_{\mathrm{LSR}} \sim -4 \, \mathrm{km \, s^{-1}}$ for Source A. For both regions, the spectral shapes with peaks at $V_{\mathrm{LSR}} \sim 9 \, \mathrm{km \, s^{-1}}$ are similar between the ^{12}CO and ^{13}CO ($J = 1$–0) lines, although the ^{12}CO ($J = 2$–1) lines match the other two
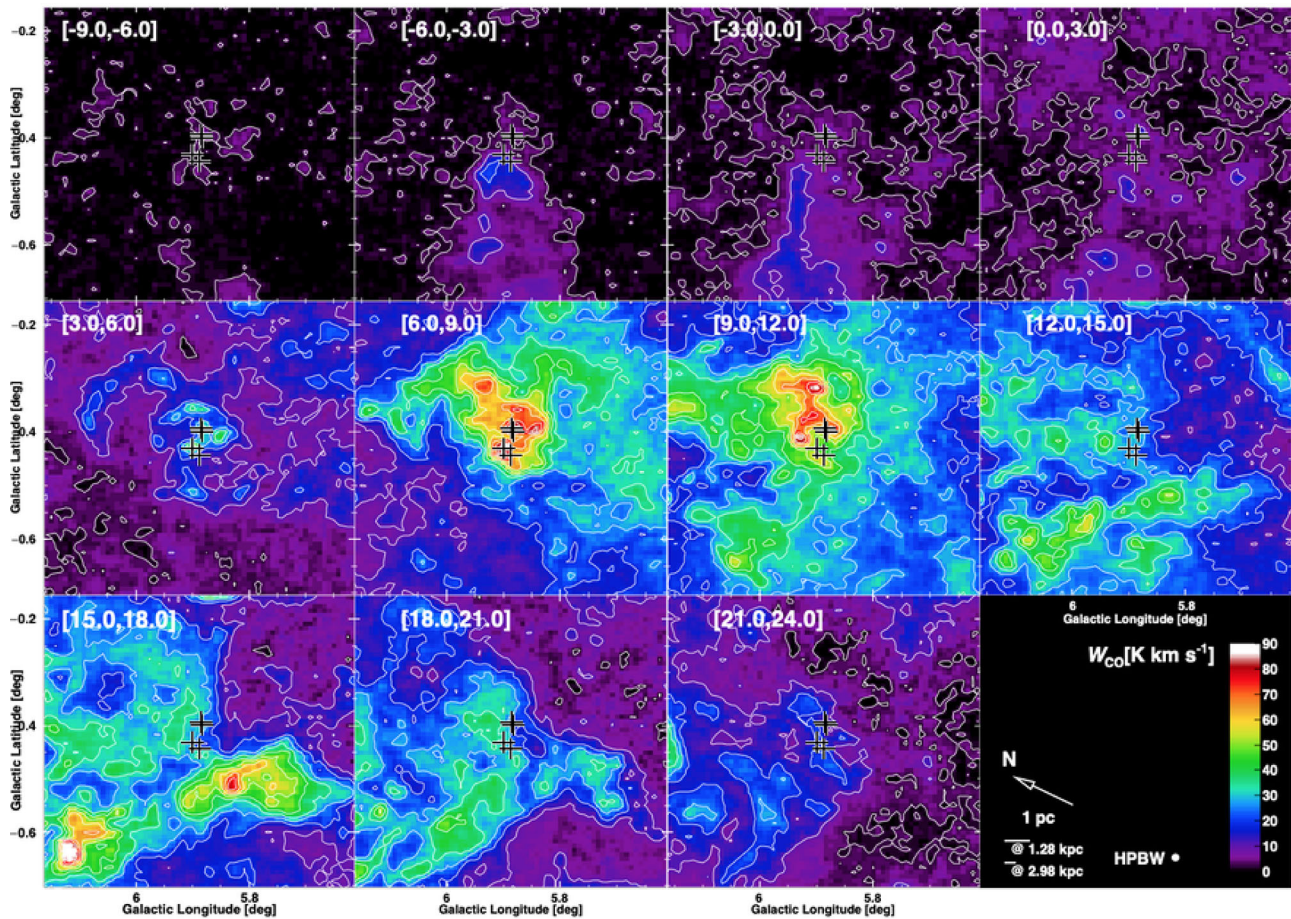
Fig. 3. Velocity channel map obtained with the Mopra ^{12}CO ($J = 1$–0) data. The integrated velocity range of each panel is 3 km s^{-1}. The lowest contour level is 5σ; the others are drawn in 20σ steps. The crosses represent the positions of the exciting sources A–D.
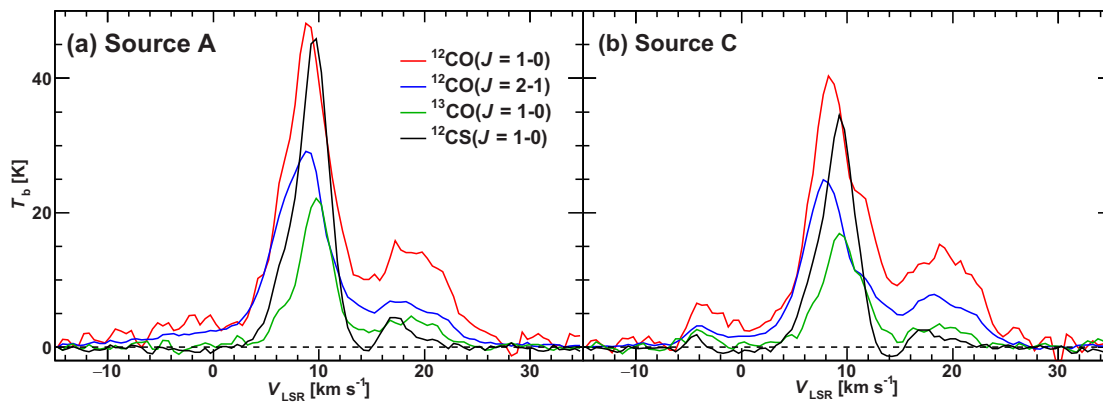
Fig. 4. Spectra toward (a) Source A and (b) Source C: ^{12}CO ($J = 1$–0, $J = 2$–1) and ^{13}CO ($J = 1$–0) spectra obtained by the NANTEN2 observation and the ^{12}CS ($J = 1$–0) spectrum obtained by the Mopra observation (Nicholas et al. 2012). The ^{12}CS ($J = 1$–0) spectrum is scaled by a factor of 10.

$J = 1$–0 lines less; the intensity of the ^{12}CO ($J = 2$–1) lines tends to be higher at $V_{\rm LSR} \lesssim 9$ km s^{-1} but lower at $V_{\rm LSR} \gtrsim 9$ km s^{-1}. In the same figure, we overlay the ^{12}CS ($J = 1$–0) line toward Sources A and C, whose data were used in a previous study of the molecular clouds in the

W 28 A2 region (Nicholas et al. 2012). Since the CS line has a higher critical density than the CO line, the spectrum traces more the emission from the high-density region, where the ^{12}CO spectrum is often saturated due to the self absorption. For easier comparison of the spectral shape
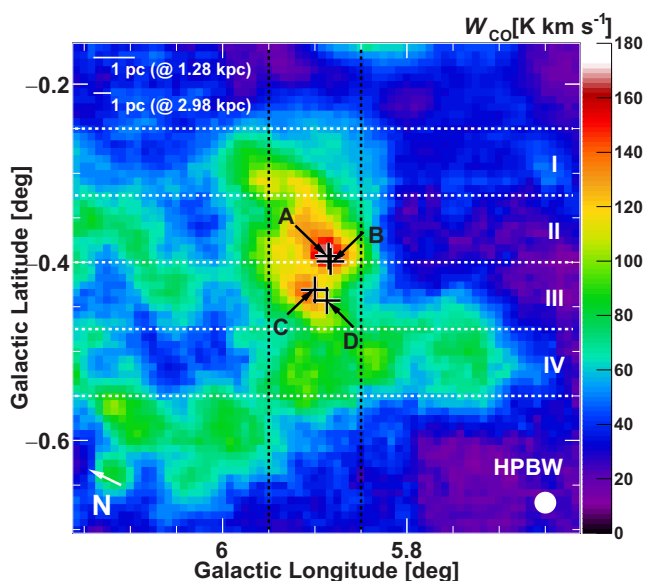
Fig. 5. Velocity-integrated intensity map of the NANTEN2 ^{12}CO (J = 2–1) data. The integrated velocity range is from -10 to $+30 \, \mathrm{km \, s^{-1}}$. The crosses represent the positions of the exciting sources A–D. The white dotted lines indicate the integrated latitude range of the position–velocity diagram shown in figure 6. The black dotted lines indicate the integrated longitude range of the position–velocity diagram shown in figure 7.

with the other ^{12}CO lines, the intensity of the ^{12}CS (J = 1–0) line is scaled by a factor of 10. In both regions, the peak velocities of the ^{12}CS line tend to be blueshifted compared to the ^{12}CO lines, and are almost consistent with the optically thin ^{13}CO (J = 1–0) spectrum. These results suggest self absorption in the ^{12}CO spectra by the dense gas in the $+9 \, \mathrm{km \, s^{-1}}$ cloud.

3.2 Velocity structure

Figure 5 shows a velocity-integrated ($-10 \, \mathrm{km \, s^{-1}} < V_{\mathrm{LSR}} < +30 \, \mathrm{km \, s^{-1}}$) intensity map of the NANTEN2 ^{12}CO (J = 2–1) data. We have separated the map into four regions I–IV for the different latitude ranges and made longitude–velocity diagrams for each region as shown in figure 6. In regions I–III, the highest CO emissions are found at $V_{\mathrm{LSR}} \sim 9 \, \mathrm{km \, s^{-1}}$, while region IV has a CO intensity peak at $V_{\mathrm{LSR}} \sim 16 \, \mathrm{km \, s^{-1}}$. In region III, where Sources C and D are included, the low-intensity gas for the $-4 \, \mathrm{km \, s^{-1}}$ cloud is confirmed and it is connected to the $+9 \, \mathrm{km \, s^{-1}}$ cloud with a bridging feature at $V_{\mathrm{LSR}} \sim 1 \, \mathrm{km \, s^{-1}}$. Region II, which includes Sources A and B, also shows the presence of low-intensity gas at $V_{\mathrm{LSR}} \sim -4 \, \mathrm{km \, s^{-1}}$, and it is connected to the $+9 \, \mathrm{km \, s^{-1}}$ cloud along the direction of these sources. This wing-like structure is also found on the opposite side at $V_{\mathrm{LSR}} \sim 13 \, \mathrm{km \, s^{-1}}$, just coinciding with the direction of Sources A and B. Region IV shows a distinct cloud at V_{LSR}

$\sim -4 \, \mathrm{km \, s^{-1}}$ with a relatively extended bridging feature in $5°85 \lesssim 5°97$ at $V_{\mathrm{LSR}} \sim 1 \, \mathrm{km \, s^{-1}}$. We do not find significant emission from the $-4 \, \mathrm{km \, s^{-1}}$ cloud and the associated bridging feature in region I. In addition to the wing-like structure at $V_{\mathrm{LSR}} \sim 13 \, \mathrm{km \, s^{-1}}$ in region II, the intermediate velocity components between the $+9 \, \mathrm{km \, s^{-1}}$ and $16 \, \mathrm{km \, s^{-1}}$ clouds are found in all regions, but they are extensively distributed and have more complicated velocity structure, especially for regions III and IV.

Figure 7 shows a latitude–velocity diagram of the NANTEN2 ^{12}CO (J = 2–1) to (J = 1–0) intensity ratio for the integrated longitude range from $5°85$ to $5°95$ represented by the black dotted lines in figure 5. For comparison, contours from the ^{12}CO (J = 2–1) data are superposed. We note that the intensity ratio map using the Mopra ^{12}CO data also gives a similar latitude–velocity diagram. Overall, the ratio becomes lower far away from the exciting sources A–D, as shown by the dotted lines, except for the local high intensity ratio at $(V_{\mathrm{LSR}}, b) = (\sim 5 \, \mathrm{km \, s^{-1}}, 0°25)$ and $(\sim 5 \, \mathrm{km \, s^{-1}}, 0°65)$. The intensity ratio is as high as ~ 1.0, particularly at $V_{\mathrm{LSR}} \sim 0$–$5 \, \mathrm{km \, s^{-1}}$. At $V_{\mathrm{LSR}} \sim 9 \, \mathrm{km \, s^{-1}}$, where physical correlation between the gas and the embedded stars is expected, the intensity ratio is down to ~ 0.6. The velocity with the highest intensity ratio is not consistent with that of the CO emission peak at $V_{\mathrm{LSR}} \sim 9 \, \mathrm{km \, s^{-1}}$. This is possibly due to self absorption in the rich gas of the $9 \, \mathrm{km \, s^{-1}}$ cloud, as discussed in subsection 4.2. The local CO intensity peak at $V_{\mathrm{LSR}} \sim 16 \, \mathrm{km \, s^{-1}}$, which corresponds to the main cloud in the $+16 \, \mathrm{km \, s^{-1}}$ cloud, shows an intensity ratio of ~ 0.6. At $V_{\mathrm{LSR}} \sim -4 \, \mathrm{km \, s^{-1}}$, the intensity ratio tends to be higher (~ 0.6–0.9) toward the direction of the exciting stars.

3.3 Comparison with radio continuum and infrared emissions

In order to investigate the physical correlations between the gas and the exciting stars, we made comparisons with the spatial distributions of the radio continuum emission possibly related to the UV photons radiated from the exciting stars and the $8 \, \mu \mathrm{m}$ infrared emission, mostly from the polycyclic aromatic hydrocarbons that are formed by photodissociation due to the UV radiation from the exciting stars. Here we used the NANTEN2 ^{12}CO (J = 2–1) data, which have higher sensitivity than the Mopra ^{12}CO (J = 1–0) data. Figures 8a and 8b show the distributions of the radio continuum emission obtained by VLA (image), compared to the molecular gas distributions of the NANTEN2 ^{12}CO (J = 2–1) data for the $-4 \, \mathrm{km \, s^{-1}}$ cloud and the $+9 \, \mathrm{km \, s^{-1}}$ cloud, respectively (gray contours). The white contours indicate depression areas in CO compared to the surrounding area. The CO intensity is enhanced at $(l, b) = (5°94, -0°47)$ for
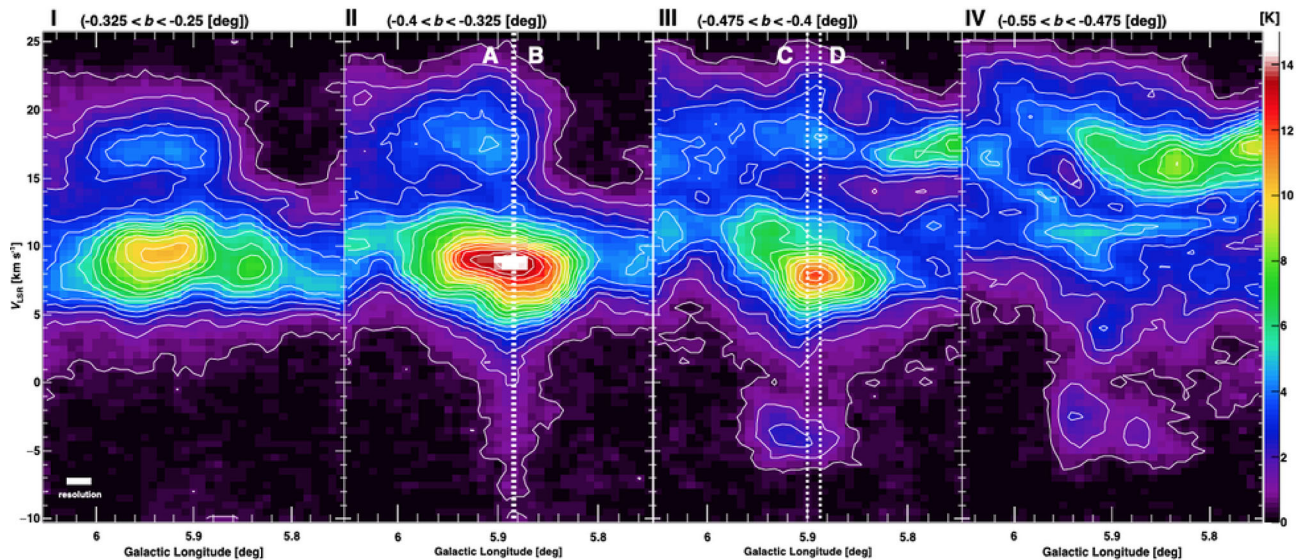
Fig. 6. Longitude–velocity diagrams of the NANTEN2 ^{12}CO ($J = 2$–1) data for regions I–IV shown in figure 5. The white dotted lines indicate the positions of the exciting sources A–D. The lowest contour corresponds to the 5σ level; the others are drawn at 6σ intervals.
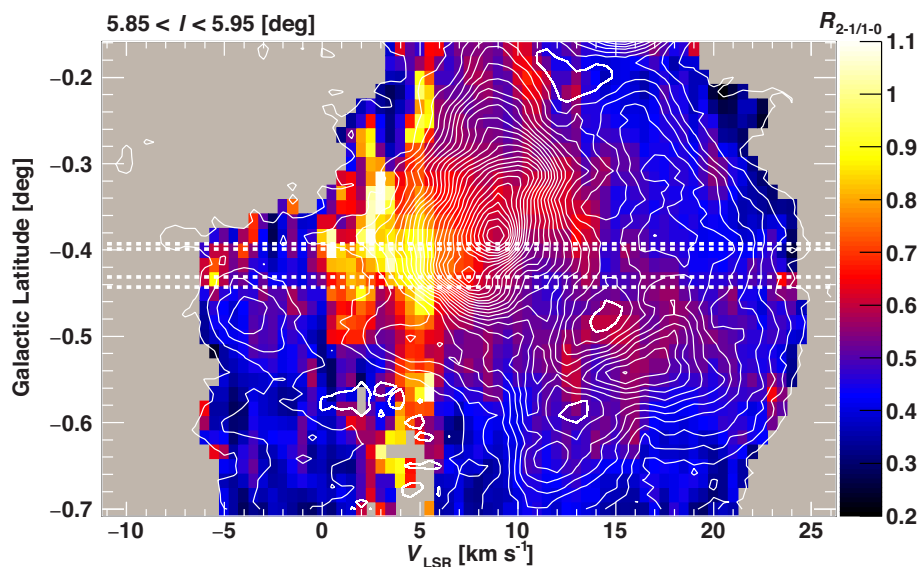
Fig. 7. Latitude–velocity diagram of the 2–1 to 1–0 intensity ratio (image) of the NANTEN2 ^{12}CO data. The integrated longitude range is from $5^\circ\!.85$ to $5^\circ\!.95$, which is shown by the black dotted lines in figure 5. The white contours indicate the NANTEN2 ^{12}CO ($J = 2$–1) data, drawn in 6σ steps from the 5σ intensity level. The thick contours show the depletion area compared to the surrounding area. The white dotted lines indicate the positions of the exciting sources A–D from top to bottom.

the $-4\,\mathrm{km\,s^{-1}}$ cloud and depressed at $(l, b) = (6^\circ\!.02, -0^\circ\!.38)$ for the $+9\,\mathrm{km\,s^{-1}}$ cloud, while conversely the radio continuum emission is depressed and enhanced, respectively. These features suggest that UV photons radiated from the massive stars are extended to the low-density medium away from the regions with rich gas. Similarly, in figures 8c and 8d, the spatial distributions of the Spitzer $8\,\mu\mathrm{m}$ infrared emission are compared to the NANTEN2 ^{12}CO ($J = 2$–1) data for the $+9\,\mathrm{km\,s^{-1}}$ and $+16\,\mathrm{km\,s^{-1}}$ clouds,

respectively. The $8\,\mu\mathrm{m}$ distribution is similar to the molecular gas distribution and delineates the outer boundary of the radio continuum emission, implying that the photodissociation is proceeding at the surface of the molecular clouds. We found spatial correspondences at $(l, b) = (5^\circ\!.92, -0^\circ\!.31)$ for the $+9\,\mathrm{km\,s^{-1}}$ cloud and $(l, b) = (5^\circ\!.75, -0^\circ\!.5)$ for the $+16\,\mathrm{km\,s^{-1}}$ cloud. These results suggest physical association of the molecular clouds of all three velocity components with the exciting sources.
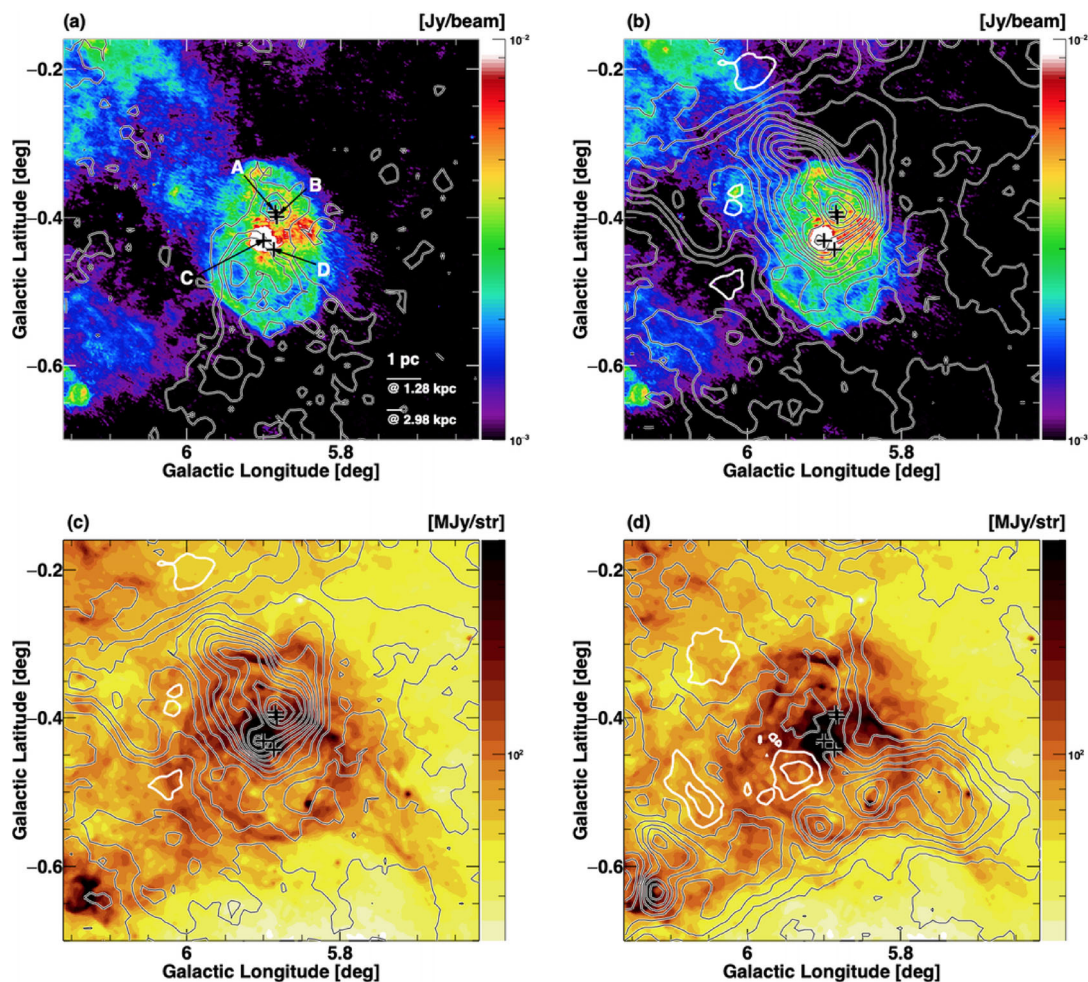
Fig. 8. Molecular gas distribution of the NANTEN2 ^{12}CO ($J = 2$–1) data (gray contours) in comparison with the VLA 20 cm radio continuum emission and Spitzer 8 μm emission (image). (a) -4 km s^{-1} cloud vs. VLA 20 cm. (b) $+9$ km s^{-1} cloud vs. VLA 20 cm. (c) $+9$ km s^{-1} cloud vs. Spitzer 8 μm. (d) $+16$ km s^{-1} cloud vs. Spitzer 8 μm. The contours start from 5σ, 15σ, and 10σ, and are drawn in 6σ, 12σ, and 11σ steps for panels (a), (b)–(c), and (d), respectively. The white contours in panels (b)–(d) indicate depression areas compared to the surrounding area. The crosses represent the positions of the exciting sources A–D.

4 Discussion

The results obtained in section 3 show the molecular gas properties in the W 28 A2 region as follows.

- The molecular clouds are extended at a scale of $\sim$5–10 pc from the center of the H II region, separated by velocity into three components with CO peaks at $V_{\rm LSR}$ ~ -4 km s^{-1}, $+9$ km s^{-1}, and $+16$ km s^{-1}. The exciting stars are embedded in gas-rich regions of the $+9$ km s^{-1} cloud, possibly forming the H II complex.
- The position–velocity diagram of the CO data shows bridging features connecting the three clouds. The wing-like structure crossing the intermediate velocity range coincides with the directions of the exciting sources A and B.
- Overall, the ^{12}CO 2–1 to 1–0 intensity ratio in the latitude–velocity diagram becomes lower far away from

the exciting sources. A high intensity ratio ($\sim$0.8–1.0) is found in the -4 km s^{-1} and $+9$ km s^{-1} clouds, but the velocity at the peak intensity ratio in the $+9$ km s^{-1} cloud is not consistent with the CO peak at $V_{\rm LSR} \sim 9$ km s^{-1}. The intensity ratio of the $+16$ km s^{-1} cloud is relatively lower ($\lesssim$0.6).
- Comparisons of the gas distributions with the radio continuum emission and the 8 μm infrared emission show spatial coincidence/anti-coincidence, suggesting physical associations between the gas and ionizing photons radiated from the exciting stars.

4.1 Spectral type of the exciting stars and the molecular gas mass

Assuming that each H II region is formed by one exciting source, we estimated their spectral types by using the

Table 1. Properties of the H II regions and expected spectral types of their exciting sources in W 28 A2.

Exciting star	H II region*	S_ν (1.4 GHz) [Jy]	$\log N_{Ly}$ [photons s^{-1}] 1.28 kpc/2.98 kpc	Spectral type[†] (ZAMS) 1.28 kpc/2.98 kpc
Source A	G005.885−00.393	0.29	46.43/47.17	∼B0.5/∼B0.5
Source B	G005.883−00.399	0.20	46.27/47.00	∼B0.5/∼B0.5
Source C	G005.900−00.431	6.09	47.75/48.49	∼O9.5/∼O7.5
Source D	G005.887−00.443	25.71	48.38/49.12	∼O8/∼O6

[*] WISE catalog name (Anderson et al. 2014).
[†] Spectral type (ZAMS; Panagia 1973).

number of Lyman continuum photons (N_{Ly}), which is derived from (Simpson & Rubin 1990)

$$N_{Ly} \simeq \frac{5.59 \times 10^{48}}{(1 + f_i)} \times T_e^{-0.45} \times \left(\frac{\nu}{\nu_5}\right)^{0.1} S_\nu D^2, \qquad (1)$$

where ν is the frequency in GHz ($\nu_5 = 5.0$ GHz) and D is the distance to the source; f_i [$\equiv$ He$^+$/(H$^+$ + He$^+$) $\simeq$ 0.65] is the helium fraction of recombination photons to excited states, and S_ν is the flux density of each H II region, whose area is determined by the threshold of the radio continuum emission shown in figure 1. This boundary is adjusted not to overlap the different H II regions and to fall within the approximate circular regions determined in the WISE catalog (Anderson et al. 2014). In estimating the flux of Source D, we masked the regions of Sources A–C to remove their contributions and interpolated with the average flux of Source D. The electron temperature T_e is assumed to be 6700 K, which is obtained from the Hα recombination line near the W 28 A2 region (Downes et al. 1980). Table 1 shows the derived S_ν and N_{Ly} at $\nu = 1.4$ GHz and the inferred spectral types of each ionizing star under the assumption of the same distance for these H II regions: $D = 1.28$ kpc (Motogi et al. 2011) and 2.98 kpc (Sato et al. 2014).

The spectral type of Source A corresponding to the position of Fieldt's star is derived to be B0.5, which is consistent with previous studies if we take into account the uncertainty arising from the different estimates and distance assumptions (e.g., Feldt et al. 2003; Motogi et al. 2011; Sato et al. 2014). Source C, whose spectral type is derived to be O7.5–9.5, coincides with the position of an X-ray protostar (Hampton et al. 2016) and is consistent with their estimates for a late O-type star. Among the four sources, Source D, having the largest N_{Ly}, shows the most massive stars with spectral type O6–8.

The molecular gas masses of the -4 km s^{-1}, $+9$ km s^{-1}, and $+16$ km s^{-1} clouds are estimated from the NANTEN2 ^{13}CO ($J = 1$–0) data: using the optical depth of the ^{13}CO ($J = 1$–0) lines derived from the assumption of local thermodynamic equilibrium (LTE), we calculated the

Table 2. Molecular gas column density and gas mass for the three velocity clouds.

Cloud	N_{H2} (peak) [10^{22} cm^{-2}]	Molecular gas mass [$M_\odot$] 1.28 kpc/2.98 kpc
-4 km s^{-1}	0.5	2.5×10^3/1.3×10^4
$+9$ km s^{-1}	4.0	3.5×10^4/1.9×10^5
$+16$ km s^{-1}	2.8	2.7×10^4/1.4×10^5

column density for ^{12}CO by adopting the ^{13}CO/^{12}CO abundance ratio 7.1×10^5 (Frerking et al. 1982). The relevant equations for calculating the gas mass are summarized in Nishimura et al. (2015). We simply derived the gas mass for the entire region investigated in this study. The obtained peak column density and gas masses for $D = 1.28$ kpc and 2.98 kpc are summarized in table 2.

Nicholas et al. (2012) measured the molecular gas column density using the CS ($J = 1$–0) line and estimated the gas mass around the four exciting sources A–D within a scale of ∼10′. The N_{H2} value obtained was 2.9×10^{23} cm^{-2}, which is much larger than our estimate even compared to the total value of the three velocity components ($N_{H2} \sim 7.3 \times 10^{22}$ cm^{-2}). The larger N_{H2} obtained in Nicholas et al. (2012) is probably due to a high-density gas tracer CS line, which has a higher critical density than the CO line. The spatial resolution of the CS ($J = 1$–0) study is ∼1′ (Nicholas et al. 2012) and thus the beam dilution effect is more significant for the NANTEN2 ^{13}CO ($J = 1$–0) data, resulting in the smaller N_{H2} in our estimate. If we assume the same distance adopted in Nicholas et al. (2012) ($D = 2$ kpc), the molecular gas mass with our CO data for the region adopted in their study (see figure 2 in Nicholas et al. 2012) is derived to be $2.3 \times 10^4 M_\odot$, which is consistent within a factor of 2.

4.2 Physical association of the molecular clouds and the exciting stars

In figure 7 we found the relatively high ^{12}CO 2–1/1–0 intensity ratio toward the exciting stars at $V_{LSR} \sim 0$–5 km s^{-1} and
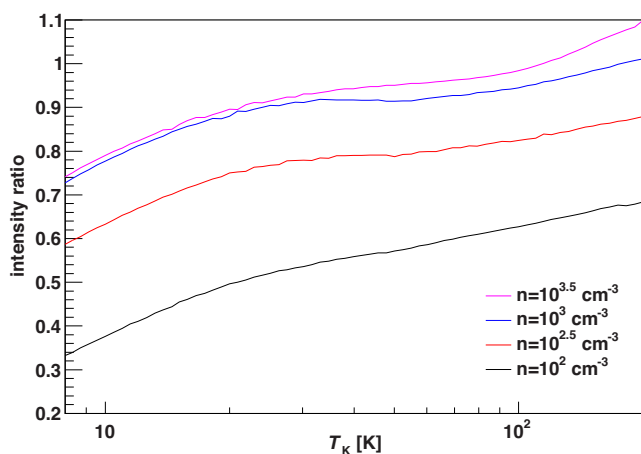
Fig. 9. Correlations between the kinetic temperature (T_k) and the ^{12}CO 2–1/1–0 intensity ratio for several molecular gas densities (n).

$\sim -4\,\mathrm{km\,s^{-1}}$. Using the NANTEN2 ^{12}CO ($J = 1$–0, $J = 2$–1) and ^{13}CO ($J = 1$–0) lines, we performed a large velocity gradient (LVG) analysis (Goldreich & Kwan 1974) under the assumptions of the abundance ratios $[^{12}\mathrm{CO}]/[\mathrm{H_2}] = 10^{-4}$ (e.g., Frerking et al. 1982; Leung et al. 1984) and $[^{12}\mathrm{C}]/[^{13}\mathrm{C}] = 77$ (Wilson & Rood 1994), and a typical velocity gradient estimated from the CO data of $dv/dr = 0.5$. We confirmed that variations of dv/dr from 0.1 to 1.0 do not significantly change the physical quantities for the target positions. The intensity ratio as a function of the kinematic temperature (T_k) for several molecular gas densities is shown in figure 9. The ratio toward the direction of the exciting stars for the $-4\,\mathrm{km\,s^{-1}}$ cloud is up to ~ 0.9 (see figure 7). From the LVG analysis, the molecular gas density for the $-4\,\mathrm{km\,s^{-1}}$ cloud is derived to be $\sim 1 \times 10^3\,\mathrm{cm^{-3}}$. Thus, the gas temperature at $V_{\mathrm{LSR}} \sim -4\,\mathrm{km\,s^{-1}}$ estimated from figure 9 is $\sim 20\,\mathrm{K}$, indicating that the $-4\,\mathrm{km\,s^{-1}}$ cloud is heated by the UV radiation from the massive stars.

For the $+9\,\mathrm{km\,s^{-1}}$ cloud, the intensity ratio in the blueshift side (at $V_{\mathrm{LSR}} \sim 5\,\mathrm{km\,s^{-1}}$) is as large as ~ 1.0, while the ratio in the redshift side is only up to ~ 0.6. The discrepancy is expected from the different spectral structure between the ^{12}CO ($J = 1$–0) and ($J = 2$–1) lines (see figure 4) and does not change significantly even if we apply the Mopra ^{12}CO ($J = 1$–0) data instead of the NANTEN2 ^{12}CO ($J = 1$–0) data. A probable effect giving the lower intensity ratio in the redshift side is self absorption by the high-density gas in the near side of the $+9\,\mathrm{km\,s^{-1}}$ cloud. This can also be suggested from the ^{12}CS ($J = 1$–0) spectrum, as described in subsection 3.1. We derived the optical depth of the ^{13}CO ($J = 1$–0) line through the molecular gas mass estimate (subsection 4.1). It is found to be 0.1–0.5 at $6 \lesssim V_{\mathrm{LSR}} \lesssim 12\,\mathrm{km\,s^{-1}}$ but is less than 0.1 at $6\,\mathrm{km\,s^{-1}}$

$\lesssim V_{\mathrm{LSR}}$, suggesting that the self absorption is not significant at $6\,\mathrm{km\,s^{-1}} \lesssim V_{\mathrm{LSR}}$. Applying the intensity ratio ~ 1.0 at $6\,\mathrm{km\,s^{-1}} \lesssim V_{\mathrm{LSR}}$, the gas density derived by the LVG analysis is $\sim 3 \times 10^3\,\mathrm{cm^{-3}}$, and thus the gas temperature inferred from figure 9 is $\sim 100\,\mathrm{K}$, suggesting a strong effect from the UV radiation from the exciting stars. According to Velázquez et al. (2002), the W 28 region has a possible large amount of clod H I in front of the H II complex. These features are also found in the ^{12}CO ($J = 3$–2) spectrum toward Source C, as shown in figure 3 in Klaassen et al. (2006). The effects of optical depths are also discussed in Wood and Churchwell (1989).

The intensity ratio of the $+16\,\mathrm{km\,s^{-1}}$ cloud overall tends to be lower the further toward the negative latitude direction from the exciting stars (see figure 7). This result may indicate that the $+16\,\mathrm{km\,s^{-1}}$ cloud is also affected by the UV radiation from Sources A–D. The spatial coincidence between the gas and the $8\,\mu$m infrared emission found in subsection 3.3 supports this indication. However, the intensity ratio (~ 0.6) is lower than the other two clouds, implying that the $+16\,\mathrm{km\,s^{-1}}$ is located furthest from the exciting stars.

W 28 A2 is located near the direction of the Galactic center, and thus multiple gas components across different spiral arms might be observed on the same line of sight. The $-4\,\mathrm{km\,s^{-1}}$ cloud is relatively isolated and no continuous gas distribution with the same velocity is found in the CO data. This result suggests that the $-4\,\mathrm{km\,s^{-1}}$ cloud is not a single component included in another spiral arm. The $+9\,\mathrm{km\,s^{-1}}$ and $+16\,\mathrm{km\,s^{-1}}$ clouds mainly cover the velocity range belonging to the Scutum or Norma arms (Reid et al. 2016). Although it is not clear that these clouds belong to either arm, we conclude that they are located in a proximal space in the same arm since they exhibit physical associations with the H II region described in subsections 3.3 and 4.4.

4.3 Molecular outflow

As described in subsection 1.2, Feldt's star, which forms an UC H II region in the W 28 A2 complex, having an extraordinary bipolar molecular outflow, has been studied extensively (e.g., Feldt et al. 2003; Leurini et al. 2015). This massive protostar corresponds to Source A, around which we find wing-like structures in the CO spectrum shown in figure 4 and the position–velocity diagram for region II in figure 6. Its broad line emission covers the velocity range from $V_{\mathrm{LSR}} \sim -15\,\mathrm{km\,s^{-1}}$ to $\sim +30\,\mathrm{km\,s^{-1}}$, centered on the systemic velocity at $V_{\mathrm{LSR}} \sim +9\,\mathrm{km\,s^{-1}}$. Using the NANTEN2 ^{12}CO ($J = 2$–1) data, we made integrated intensity maps for the blue- and redshifted components in the spectrum, as shown by the contours superposed on the VLA
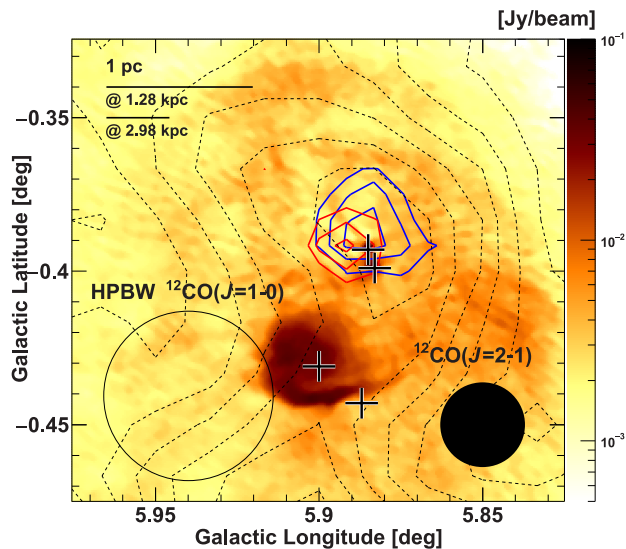
Fig. 10. Velocity-integrated maps for the wing components using the NANTEN2 ^{12}CO ($J = 2$–1) data (contours) superposed on the VLA 20 cm radio continuum emission (image). The integrated velocity ranges for the wing components are $-15\,\mathrm{km\,s^{-1}}$ to $+3\,\mathrm{km\,s^{-1}}$ (blue) and $+15\,\mathrm{km\,s^{-1}}$ to $+30\,\mathrm{km\,s^{-1}}$ (red). The contours with the dotted lines indicate the intermediate velocity component ($-1\,\mathrm{km\,s^{-1}} < V_{\mathrm{LSR}} < +4\,\mathrm{km\,s^{-1}}$) with the NANTEN2 ^{12}CO ($J = 1$–0) data, drawn in $2\,\sigma$ steps from the $5\,\sigma$ level. The beam sizes of each CO line are represented. The crosses represent the positions of the exciting sources A–D.

20 cm radio continuum emission (figure 10). The integrated velocity ranges of the blue- and redshifted components are $-15\,\mathrm{km\,s^{-1}}$ to $+3\,\mathrm{km\,s^{-1}}$ and $+15\,\mathrm{km\,s^{-1}}$ to $+30\,\mathrm{km\,s^{-1}}$, respectively. The Mopra ^{12}CO ($J = 1$–0) data show a similar wing component for the blueshift side, but we could not find the redshifted component, possibly due to its slightly lower sensitivity than the NANTEN2 ^{12}CO ($J = 2$–1) data. The image obtained clearly shows the presence of strong CO emission from the Source A position, suggesting that the broad line emission is due to molecular outflow. With the method described in subsection 4.1, the molecular gas masses of the blue- and redshifted components were derived to be $224\,M_{\odot}$ and $130\,M_{\odot}$, respectively. The lower CO intensity and gas mass of the redshift component compared with the blueshift component can be attributed to the self absorption in the near side of the $+9\,\mathrm{km\,s^{-1}}$ cloud. If we take into account the difference in the adopted distance to the clouds, this result is consistent with the gas masses obtained by Watson et al. (2007), who give $123\,M_{\odot}$ and $126\,M_{\odot}$ for the blue and red components, respectively. In the same figure, we overlay other contours representing the integrated intensity of the NANTEN2 ^{12}CO ($J = 1$–0) data for the intermediate velocity cloud ($-1\,\mathrm{km\,s^{-1}} < V_{\mathrm{LSR}} < +4\,\mathrm{km\,s^{-1}}$), to compare the extension of the CO emission with the wing-like feature due to the outflow. The Mopra ^{12}CO ($J = 1$–0) data also show a similar gas distribution at

$5\,\sigma$ significance. The low-density cloud at the intermediate velocity is more widely extended than the molecular outflows, suggesting that the broad line emission found in the spectrum and the position–velocity diagram includes the bridge component between the $-4\,\mathrm{km\,s^{-1}}$ and $+9\,\mathrm{km\,s^{-1}}$ clouds, in addition to the wing component originating from the massive stars.

4.4 Triggering mechanisms of high-mass star formation

We found physical associations between the high-mass stars and the surrounding molecular gas separated into the three velocity components. Here we discuss possible scenarios for the formation of the high-mass stars, especially focusing on the triggering mechanisms introduced in subsection 1.1.

Figure 11 shows longitude–velocity diagrams obtained with the Mopra ^{12}CO ($J = 1$–0) data (image) and ^{13}CO ($J = 1$–0) data (contours), whose integrated latitude ranges are represented by the horizontal dotted lines in figure 12, where the distributions of the Mopra ^{13}CO ($J = 1$–0) (contours) and the VLA 20 cm radio continuum emission (image) are compared in a velocity channel map. Panel (c) in figure 11, showing the gas structure around the exciting sources C/D, mainly consists of the highest CO intensity peak with a wide velocity range toward the exciting source C, and clouds at $l = 5°.87$ showing an elongated structure toward the south direction (see the $8\,\mathrm{km\,s^{-1}} < V_{\mathrm{LSR}} < 9\,\mathrm{km\,s^{-1}}$ component in figure 12). Panel (b) corresponds to the intermediate area between Sources C/D and A/B, having the velocity structure extended to the positive longitude direction and the relatively diffuse emission at $l = 5°.87$. In the area of the diffuse gas component at $l = 5°.87$, strong radio continuum emission with a flow-like structure is detected, showing an anti-correlation with the gas component (see $7\,\mathrm{km\,s^{-1}} < V_{\mathrm{LSR}} < 10\,\mathrm{km\,s^{-1}}$ in figure 12). Panel (a), corresponding to the gas around Sources A/B, has three peaks at $l = 5°.84$, $5°.8$, and $5°.93$. Although physical association among these three components is not clear, their velocity structures (peak velocity and covering velocity range) are apparently different. If the expanding gas motion by the UV radiation dominantly affects the gas distribution, these position–velocity diagrams expect to show circular structure as illustrated in figure 8 of Torii et al. (2015). However, we do not find such circular structures in either diagram. It is difficult to attribute the distinct multiple velocity components to the expanding motion of the H II gas. In addition, the expanding scenario cannot explain the formation process of the first-born exciting star. We infer that
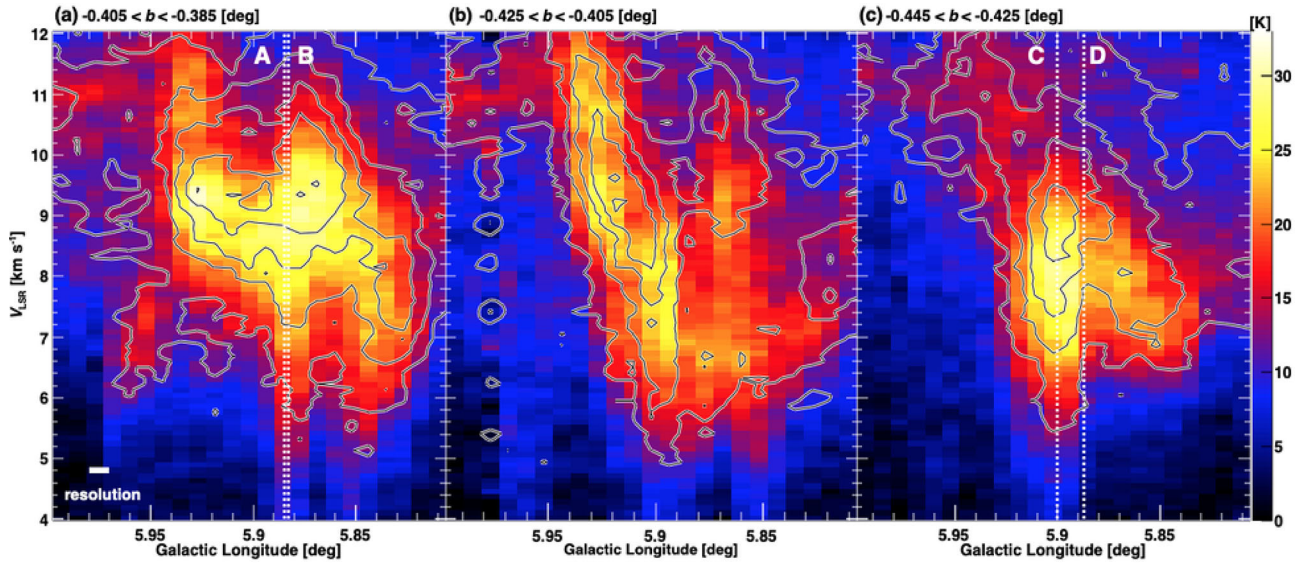
Fig. 11. Longitude–velocity diagram for the $+9\,\mathrm{km\,s^{-1}}$ cloud obtained with the Mopra ^{12}CO $(J = 1–0)$ (image) and ^{13}CO $(J = 1–0)$ (contour) data. The integrated latitude ranges are (a) $−0°405 < b < −0°385$, (b) $−0°425 < b < −0°405$, and (c) $−0°445 < b < −0°425$ as shown in figure 12. The contours are drawn in 3σ steps from the 3σ intensity level. The dotted line represents the positions of the exciting sources A–D.

the velocity differences among the clouds are not produced by the expanding motions by the exciting stars, but rather existed prior to the formation of the high-mass stars.

Figures 13a and 13b show comparisons of the velocity-integrated intensity maps of the NANTEN2 ^{12}CO $(J = 2–1)$ data for the $−4\,\mathrm{km\,s^{-1}}$ and $+9\,\mathrm{km\,s^{-1}}$ clouds, and the $−4\,\mathrm{km\,s^{-1}}$ and $+16\,\mathrm{km\,s^{-1}}$ clouds, respectively. We found multiple complementary gas distributions such as toward $(l, b) = (5°94, −0°48)$ and $(5°95, −0°60)$; the positions of the CO peaks in the $−4\,\mathrm{km\,s^{-1}}$ cloud correspond to the depression areas in the other clouds. The Mopra ^{12}CO $(J = 1–0)$ data also showed similar gas distributions. From table 2, the total gas mass of the $−4\,\mathrm{km\,s^{-1}}$ and $+9\,\mathrm{km\,s^{-1}}$ clouds in the case of a distance of 1.28 kpc is $\sim 3.8 \times 10^4\,M_\odot$, and that of the $−4\,\mathrm{km\,s^{-1}}$ and $+16\,\mathrm{km\,s^{-1}}$ clouds is $\sim 3.0 \times 10^4\,M_\odot$. The required gas mass (M) to bind the two clouds is estimated from the balance between the kinetic energy and the potential energy: $M = rv^2/2G$, where v is the relative velocity between the two clouds, and G is the gravitational constant. Under the assumption of a cloud radius of $r = 5$ pc, these gas masses are calculated to be $M \sim 9.8 \times 10^4\,M_\odot$ and $M \sim 2.3 \times 10^5\,M_\odot$, respectively, which are larger than the estimated total gas masses. Even if we assume that the distance is 2.98 kpc and the cloud radius is 11.5 pc (increasing proportionally to the distance), the tendency of the binding mass to be larger than the total gas mass does not change. These results indicate that the two clouds are not gravitationally bound due to the large velocity difference of up to $\sim 13\,\mathrm{km\,s^{-1}}$ and $\sim 20\,\mathrm{km\,s^{-1}}$. Most of the gas in the $−4\,\mathrm{km\,s^{-1}}$ and $+16\,\mathrm{km\,s^{-1}}$ clouds

is extended toward the negative latitude direction compared to the $+9\,\mathrm{km\,s^{-1}}$ cloud, presumably outside the influence driven by Sources A–D (see the contours in the position–velocity diagram of figure 7), and thus it is difficult to expect that the simple expanding gas motion from the $+9\,\mathrm{km\,s^{-1}}$ cloud generates the observed gas structure. These results suggest incidental collisions of the $−4\,\mathrm{km\,s^{-1}}$ and $+9/+16\,\mathrm{km\,s^{-1}}$ clouds rather than expanding gas motion from the $+9\,\mathrm{km\,s^{-1}}$ cloud.

The $−4\,\mathrm{km\,s^{-1}}$ and $+9\,\mathrm{km\,s^{-1}}$ clouds overlap mainly toward the regions with molecular gas around Sources A–D. Whereas the $+9\,\mathrm{km\,s^{-1}}$ cloud includes relatively highly dense gas at $(l, b) \sim (5°93, −0°30)$, the $−4\,\mathrm{km\,s^{-1}}$ cloud does not show significant CO emission from this area, where we do not find possible exciting sources. These results are not inconsistent with the triggering scenario to form Sources A–D by a collision between the $−4\,\mathrm{km\,s^{-1}}$ and $+9\,\mathrm{km\,s^{-1}}$ clouds. The bridging feature between the two clouds seen in figure 6 is a characteristic feature of cloud–cloud collision as reported in many studies (see the references in subsection 1.1). The high ^{12}CO $J = 2–1$ to 1–0 intensity ratio toward the exciting sources for the $−4\,\mathrm{km\,s^{-1}}$ and $+9\,\mathrm{km\,s^{-1}}$ clouds supports the physical correlation between the stars and the two clouds. Partly complementary gas distributions between the $−4\,\mathrm{km\,s^{-1}}$ and $+9\,\mathrm{km\,s^{-1}}$ clouds, and the $−4\,\mathrm{km\,s^{-1}}$ and $+16\,\mathrm{km\,s^{-1}}$ clouds, suggest physical interactions among these clouds. On the other hand, we do not find a clear correlation between the $+9\,\mathrm{km\,s^{-1}}$ and $+16\,\mathrm{km\,s^{-1}}$ clouds from the cloud morphology. Although the $+16\,\mathrm{km\,s^{-1}}$ cloud would be part of the clouds forming the W 28 A2 region, it would
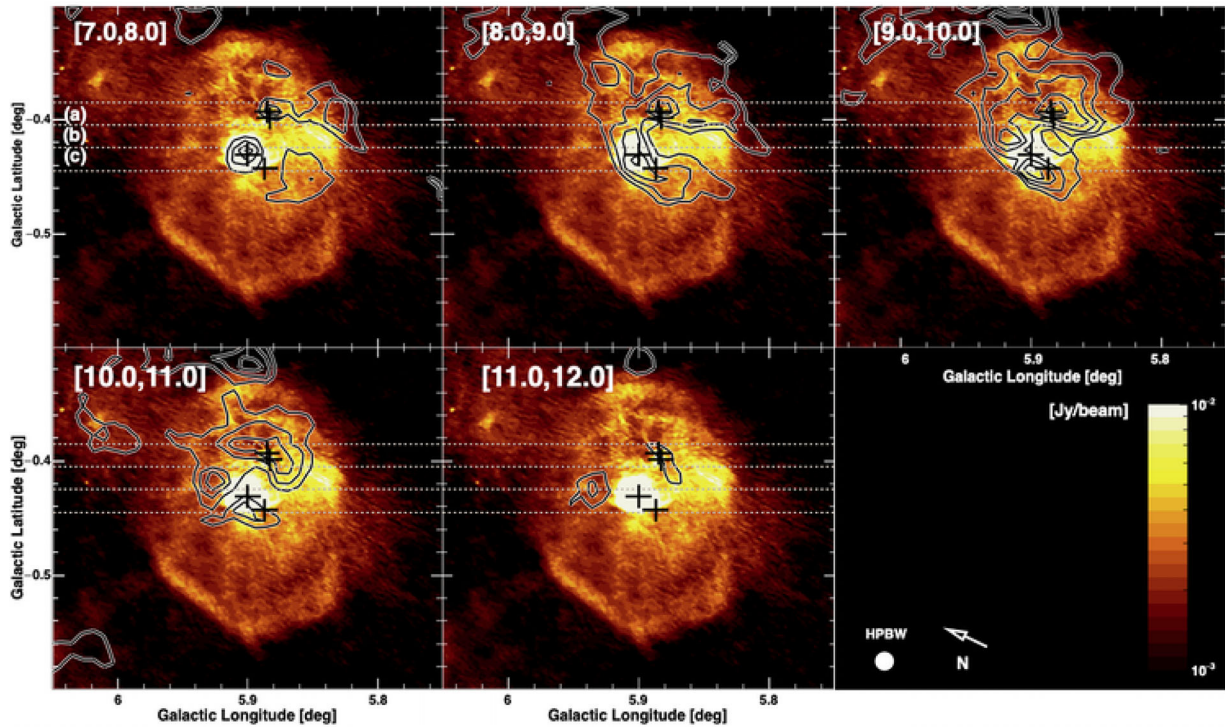
Fig. 12. Velocity channel map for the $+9\,\mathrm{km\,s^{-1}}$ cloud using the Mopra ^{13}CO ($J = 1$–0) data (contour) compared to the VLA 20 cm radio continuum emission (image). The contours are drawn in 2σ steps from the 3σ level. The regions (a)–(c) separated by the horizontal dotted lines correspond to the integrated latitude ranges for the position–velocity diagrams shown in figure 11. The crosses represent the positions of the exciting sources A–D.
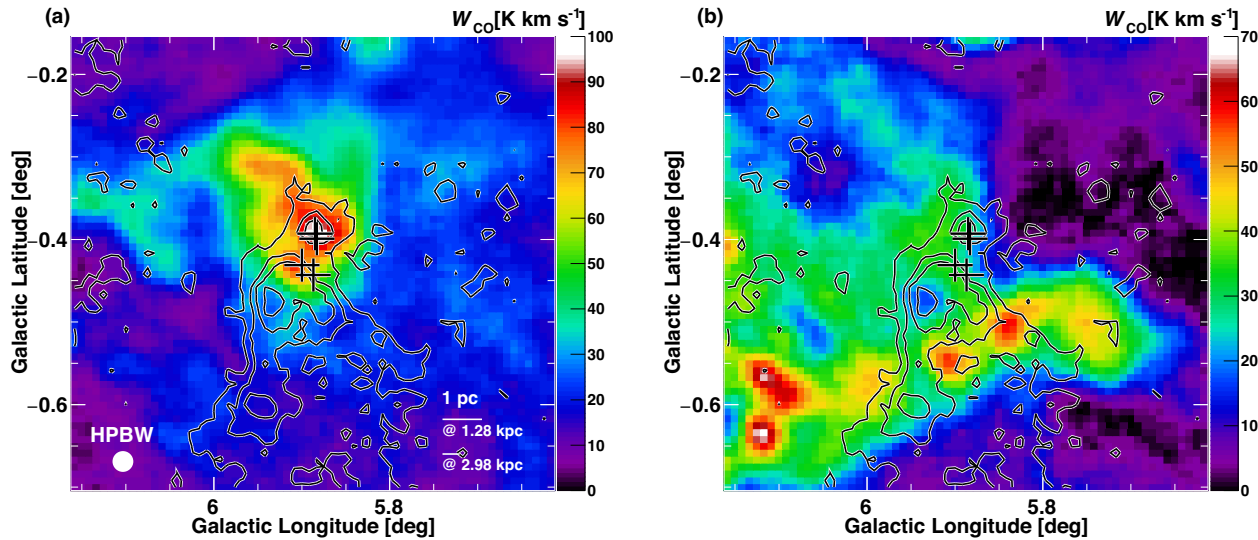

Fig. 13. Comparisons of the two clouds using the velocity-integrated intensity maps of the NANTEN2 ^{12}CO ($J = 2$–1) data. (a) $-4\,\mathrm{km\,s^{-1}}$ cloud (contour) and $+9\,\mathrm{km\,s^{-1}}$ cloud (image). (b) $-4\,\mathrm{km\,s^{-1}}$ cloud (contour) and $+16\,\mathrm{km\,s^{-1}}$ cloud (image). The contour levels for the $-4\,\mathrm{km\,s^{-1}}$ cloud are as in figure 8a. The crosses represent the positions of the exciting sources A–D.

be far away from the exciting stars compared to the other two clouds, as discussed in subsection 4.2.

From the above discussion, we propose that a cloud–cloud collision between the $-4\,\mathrm{km\,s^{-1}}$ and $+9\,\mathrm{km\,s^{-1}}$ clouds

triggered the formation of the high-mass stars in the H II region of W 28 A2. Figure 14 shows a schematic image representing the configuration of the three velocity clouds and the massive stars in the W 28 A2 region. A collision
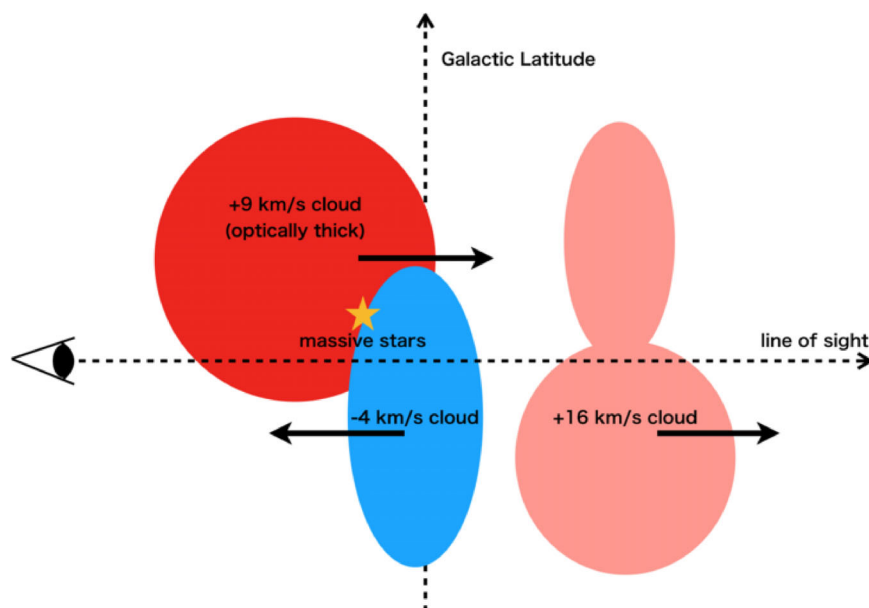
Fig. 14. Schematic image of the W 28 A2 region.

on the line of sight between the two clouds is occurring, giving a trigger for the formations of Sources A–D. The $+16\,\mathrm{km\,s^{-1}}$ cloud is positioned at the furthest side from the exciting stars among the three clouds; the $+16\,\mathrm{km\,s^{-1}}$ cloud partly shows a complementary gas distribution with the $-4\,\mathrm{km\,s^{-1}}$ cloud, as shown in figure 13b, and thus one expects a physical interaction in the past. The $-4\,\mathrm{km\,s^{-1}}$ cloud is now colliding with the $+9\,\mathrm{km\,s^{-1}}$ cloud just behind the high-density regions of the $+9\,\mathrm{km\,s^{-1}}$ cloud. This is consistent with the picture of the obscuration of the $+9\,\mathrm{km\,s^{-1}}$ cloud, possibly due to the strong self-absorption toward the W 28 A2 region, as suggested from the spectral features obtained in this study and a previous molecular cloud observation (Klaassen et al. 2006).

4.5 Comparison with other cloud–cloud collision candidates

Most of the candidates for high-mass star or cluster formation trigged by cloud–cloud collision show the presence of complementary gas distribution, because the collision of a smaller cloud creates a hole in the larger cloud (Habe & Ohta 1992; Takahira et al. 2014). However, we do not find a clear complementary gas distribution toward the exciting sources A–D between the $-4\,\mathrm{km\,s^{-1}}$ and $+9\,\mathrm{km\,s^{-1}}$ clouds. On the contrary, the CO intensities toward Sources A–D between the two clouds provides a positive intensity correlation (see figure 13a). If the collision is an early stage (cf. Habe & Ohta 1992), a hole due to the collision has not been created, and thus the complementary gas distribution may not be found. The CO destruction by UV radiation from

the massive stars is not yet significant. Such cloud properties have already been suggested for the Galactic super star clusters RCW 38 (Fukui et al. 2016) and NGC 6334 (Fukui et al. 2018b).

RCW 38 is one of the youngest star-forming regions, where ~ 20 O-type stars are located. Fukui et al. (2016) suggested that the formation of high-mass stars in the cluster was triggered by cloud collision about 0.1 Myr ago. These massive stars are localized in the overlap region between the two clouds, which are connected by a bridging feature in the velocity space. The rich gas around the massive stars suggests that the ionization is not significant yet, and the less complementary gas distribution implies an early stage of the collision. This interpretation is also supported by Torii et al. (2021), who suggested a young dynamical timescale ($<1000\,\mathrm{yr}$) for the starless cores in RCW 38, and the massive condensations in the cluster probably formed via cloud–cloud collision. Fukui et al. (2018b) found that the molecular gas toward the high-mass stars in NGC 6334 does not show a complementary gas distribution and has a positive intensity correlation between the colliding clouds. The velocity difference between the colliding clouds is as high as $\sim 12\,\mathrm{km\,s^{-1}}$, which is similar to that of the $-4\,\mathrm{km\,s^{-1}}$ and $+9\,\mathrm{km\,s^{-1}}$ clouds in the W 28 A2 region. Their large relative velocity indicates that the gas is accumulated by the collision in a short time, possibly leading to rapid formation of the high-mass stars.

We also mention a possible correlation of the peak gas column density with the relative velocity between the colliding clouds and the number of massive stars for regions triggered by cloud–cloud collision (Enokiya et al. 2021).

The peak column density for the W 28 A2 region obtained in this study is $\sim 4 \times 10^{22}\,\mathrm{cm}^{-2}$ (for the $+9\,\mathrm{km\,s}^{-1}$ cloud) and the relative velocity is $\sim 13\,\mathrm{km\,s}^{-1}$ (between the $-4\,\mathrm{km\,s}^{-1}$ and $+9\,\mathrm{km\,s}^{-1}$ clouds) if we assume a collision along the line of sight. The W 28 A2 region holds at least four high-mass stars. Our results are nearly consistent with their statistical study. Even if we assume that the $+9\,\mathrm{km\,s}^{-1}$ cloud has a column density few times larger than obtained from the CS line observation (Nicholas et al. 2012), the consistency with the statistical study does not change. These results support star formation in the W 28 A2 region triggered by cloud–cloud collision.

5 Summary

We have investigated the distributions and properties of the molecular gas in the H II region W 28 A2 using ^{12}CO and ^{13}CO ($J = 1$–0) and ^{12}CO ($J = 2$–1) data obtained with the NANTEN2 and Mopra telescopes. The molecular clouds are extended within $\sim$5–10 pc from the center of the H II region, consisting of the three velocity components with the CO intensity peaks at $V_{\mathrm{LSR}} \sim -4\,\mathrm{km\,s}^{-1}$, $9\,\mathrm{km\,s}^{-1}$, and $16\,\mathrm{km\,s}^{-1}$. The position–velocity diagram of the CO data shows bridging features connecting the three clouds and coinciding with the directions of the exciting sources. Comparisons of the gas distributions with the radio continuum emission and $8\,\mu\mathrm{m}$ infrared emission show spatial coincidence/anti-coincidence, suggesting physical associations between the gas and the exciting sources. The spectral type of the exciting stars are estimated to be O6–B0.5.

The obtained ^{12}CO $J = 2$–1 to 1–0 intensity ratio is $\gtrsim 0.8$ for the $-4\,\mathrm{km\,s}^{-1}$ and $+9\,\mathrm{km\,s}^{-1}$ clouds, suggesting physical associations with the exciting sources. At the CO intensity peak in the $+9\,\mathrm{km\,s}^{-1}$ cloud, where the exciting stars are possibly embedded, the intensity ratio is relatively lower due to self absorption by the high-density clouds. The position–velocity diagram does not show a feature expected in the case of simple expanding gas motion from the exciting source. The exciting sources are located toward the overlapping region of the $-4\,\mathrm{km\,s}^{-1}$ and $+9\,\mathrm{km\,s}^{-1}$ clouds, and the bridging features between the two clouds are found toward this direction. These gas properties are similar to the Galactic massive star clusters RCW 38 and NGC 6334, where an early stage of cloud collision triggering star formation is suggested. The formation of high-mass stars in the H II regions of W 28 A2 can be interpreted as a scenario of cloud–cloud collision.

Acknowledgement

References

Acord, J. M., Churchwell, E., & Wood, D. O. S. 1998, ApJ, 495, L107

Anderson, L. D., Bania, T. M., Balser, D. S., Cunningham, V., Wenger, T. V., Johnstone, B. M., & Armentrout, W. P. 2014, ApJS, 212, 1

Beaumont, C. N., & Williams, J. P. 2010, ApJ, 709, 791

Braiding, C., et al. 2015, PASA, 32, e020

Braiding, C., et al. 2018, PASA, 35, e029

Burton, M. G., et al. 2013, PASA, 30, e044

Churchwell, E., et al. 2006, ApJ, 649, 759

Churchwell, E., et al. 2007, ApJ, 670, 428

Dale, J. E., Ngoumou, J., Ercolano, B., & Bonnell, I. A. 2013, MNRAS, 436, 3430

Deharveng, L., Lefloch, B., Zavagno, A., Caplan, J., Whitworth, A. P., Nadeau, D., & Martín, S. 2003, A&A, 408, L25

Dewangan, L. K. 2017, ApJ, 837, 44

Downes, D., Wilson, T. L., Bieging, J., & Wink, J. 1980, A&AS, 40, 379

Elmegreen, B. G. 1998, in ASP Conf. Ser. 148, Origins, ed. C. E. Woodward et al. (San Francisco: ASP), 150

Elmegreen, B. G., & Lada, C. J. 1977, ApJ, 214, 725

Enokiya, R., et al. 2018, PASJ, 70, S49

Enokiya, R., Torii, K., & Fukui, Y. 2021, PASJ, 73, S75

Feldt, M., et al. 2003, ApJ, 599, L91

Fish, V. L., Reid, M. J., Wilner, D. J., & Churchwell, E. 2003, ApJ, 587, 701

Frerking, M. A., Langer, W. D., & Wilson, R. W. 1982, ApJ, 262, 590

Fujita, S., et al. 2019, ApJ, 872, 49

Fukui, Y., et al. 2016, ApJ, 820, 26

Fukui, Y., et al. 2018a, ApJ, 859, 166

Fukui, Y., et al. 2018b, PASJ, 70, S41

Furukawa, N., Dawson, J. R., Ohama, A., Kawamura, A., Mizuno, N., Onishi, T., & Fukui, Y. 2009, ApJ, 696, L115

Goldreich, P., & Kwan, J. 1974, ApJ, 189, 441

Goudis, C. 1976, Ap&SS, 40, 91

Habe, A., & Ohta, K. 1992, PASJ, 44, 203

Hampton, E. J., Rowell, G., Hofmann, W., Horns, D., Uchiyama, Y., & Wagner, S. 2016, J. High Energy Astrophys., 11, 1

Hanabata, Y., et al. 2014, ApJ, 786, 145

Hayashi, K., et al. 2018, PASJ, 70, S48

Hosokawa, T., & Inutsuka, S. 2006, ApJ, 646, 240

Hunter, T. R., Brogan, C. L., Indebetouw, R., & Cyganowski, C. J. 2008, ApJ, 680, 1271

Inoue, T., & Fukui, Y. 2013, ApJ, 774, L31

Klaassen, P. D., Plume, R., Ouyed, R., von Benda-Beckmann, A. M., & Di Francesco, J. 2006, ApJ, 648, 1079

Kohno, M., et al. 2021, PASJ, 73, S338

Leung, C. M., Herbst, E., & Huebner, W. F. 1984, ApJS, 56, 231

Leurini, S., et al. 2015, A&A, 584, A70

Loren, R. B. 1979, ApJ, 234, L207

Milne, D. K., & Hill, E. R. 1969, Austr. J. Phys., 22, 211

Motogi, K., Sorai, K., Habe, A., Honma, M., Kobayashi, H., & Sato, K. 2011, PASJ, 63, 31

Nicholas, B. P., Rowell, G., Burton, M. G., Walsh, A. J., Fukui, Y., Kawamura, A., & Maxted, N. I. 2012, MNRAS, 419, 251

Nishimura, A., et al. 2015, ApJS, 216, 18

Nishimura, A., et al. 2018, PASJ, 70, S42

Ohama, A., et al. 2010, ApJ, 709, 975

Panagia, N. 1973, AJ, 78, 929

Reid, M. J., Dame, T. M., Menten, K. M., & Brunthaler, A. 2016, ApJ, 823, 77

Sano, H., et al. 2018, PASJ, 70, S43

Sano, H., et al. 2021, PASJ, 73, S62

Sato, M., et al. 2014, ApJ, 793, 72

Simpson, J. P., & Rubin, R. H. 1990, ApJ, 354, 165

Su, Y.-N., Liu, S.-Y., Chen, H.-R., & Tang, Y.-W. 2012, ApJ, 744, L26

Tachihara, K., Gratier, P., Sano, H., Tsuge, K., Miura, R. E., Muraoka, K., & Fukui, Y. 2018, PASJ, 70, S52

Takahira, K., Tasker, E. J., & Habe, A. 2014, ApJ, 792, 63

Tan, J. C., Beltrán, M. T., Caselli, P., Fontani, F., Fuente, A., Krumholz, M. R., McKee, C. F., & Stolte, A. 2014, in Protostars and Planets VI, ed. H. Beuther et al. (Tucson: University of Arizona Press), 149

Torii, K., et al. 2015, ApJ, 806, 7

Torii, K., et al. 2017, ApJ, 835, 142

Torii, K., Tokuda, K., Tachihara, K., Onishi, T., & Fukui, Y. 2021, PASJ, in press (arXiv:1907.07358)

Tsuge, K., et al. 2019, ApJ, 871, 44

Velázquez, P. F., Dubner, G. M., Goss, W. M., & Green, A. J. 2002, AJ, 124, 2145

Watson, C., Churchwell, E., Zweibel, E. G., & Crutcher, R. M. 2007, ApJ, 657, 318

Wilson, T. L., & Rood, R. 1994, ARA&A, 32, 191

Wood, D. O. S., & Churchwell, E. 1989, ApJS, 69, 831

Zavagno, A., Deharveng, L., Brand, J., Massi, F., Caplan, J., Comerón, F., & Lefloch, B. 2005, in IAU Symp. 227, Massive Star Birth: A Crossroads of Astrophysics, ed. R. Cesaroni (Cambridge: Cambridge University Press), 346

Zinnecker, H., & Yorke, H. W. 2007, ARA&A, 45, 481